Journal of Materials Science & Technology 162 (2023) 25–37

Contents lists available at ScienceDirect

Journal of Materials Science & Technology

journal homepage: www.elsevier.com/locate/jmst

Research Article

Hierarchical strain band formation and mechanical behavior of a heterostructured dual-phase material

Zhongkai Li[a,*], Yujie Liu[a], Yanfei Wang[b], Jun Hu[c], Lei Xu[d], Jianjun Wang[a], Chunming Liu[a], Yuntian Zhu[e,*]

[a] Key Laboratory for Anisotropy and Texture of Materials of Ministry of Education, Northeastern University, Shenyang 110819, China
[b] Department of Mechanics and Engineering Science, College of Engineering, Peking University, Beijing 100871, China
[c] The State Key Laboratory of Rolling and Automation, Northeastern University, Shenyang 110819, China
[d] Shi-Changxu Innovation Center for Advanced Materials, Institute of Metal Research, Chinese Academy of Sciences, Shenyang 110016, China
[e] Department of Materials Science and Engineering, City University of Hong Kong, Hong Kong, China

ARTICLE INFO

Article history:
Received 17 January 2023
Revised 14 February 2023
Accepted 18 February 2023
Available online 20 April 2023

Key words:
Heterostructured materials
Strain bands
Strain gradient
Hetero-deformation induced hardening

ABSTRACT

Dispersive strain bands have been reported as a characteristic deformation feature of heterostructured materials, which helps to improve ductility. However, their formation mechanism is still not well understood. Here we report the formation of dispersed strain bands through dual-level hierarchical strain banding and its effect on the mechanical behavior of a heterostructured Fe-40Cu model material. Specifically, deformation started by the formation and propagation of dispersed microscale strain bands in the heterostructured Fe-40Cu material. High strain gradient was generated within the microscale strain bands during their propagation and was accommodated by the accumulation of geometrically necessary dislocations (GNDs). The dispersed microscale strain bands were not uniformly distributed, but instead grouped together to form macroscale strain bands that were uniformly distributed over the entire gage section to accommodate the majority of the applied strain. The formation of this dual-level hierarchical strain bands prevented the formation of large strain localization to fail the sample prematurely. It was also found that increasing the strain hardening capacity of soft copper zones provides more room for the accumulation of GNDs, resulting in higher constraint to microscale strain band propagation and consequently higher ductility. These observations suggest the possibility of tailoring microscale strain bands to optimize tensile performance of heterostructured materials.

1. Introduction

Heterostructured (HS) materials are an emerging class of materials with superior strength-ductility combination, which is unachievable for their conventional homogeneous counterparts [1,2]. A broad range of heterostructures have been reported, including heterogeneous lamella structure (HLS) [3–6], gradient structure [7–12], layered structure [13–15], dual phase structure [16,17], harmonic structure [18–21], etc. All of the heterostructures share one common design principle—soft zones or layers are constrained by hard matrix or layers.

Dramatic mechanical incompatibility between the mutually constrained hard matrix and soft zones leads to hetero-deformation among these HS zones [1]. The hetero-deformation between hard and soft zones leads to the excellent strength-ductility combination of HS materials. At the early stage of tensile deformation, the soft zones start plastic deformation first while the hard zones remain elastic. Geometrically necessary dislocations (GNDs) in soft zones pile up against the HS zone interfaces to sustain this hetero-deformation, creating long-range back stress in soft zones and forward stress in the hard matrix [22]. The interaction between back stresses and forward stresses produces hetero-deformation induced (HDI) stress that makes HS materials stronger than the prediction by the role-of-mixtures [4,15,23]. After HS materials start yielding, hetero-deformation proceeds as strain partition grows between hard and soft zones [3]. As a result, strain gradient grows near the interfaces with the applied strain to maintain continuity at HS zone interfaces. The growing strain gradient leads to further generation of GNDs, raising back stress in soft zones and forward stress in hard matrix. This produces extra strain hardening, i.e., HDI hardening, that helps with retaining ductility.

* Corresponding authors.
E-mail addresses: danielli@stumail.neu.edu.cn (Z. Li), yuntizhu@cityu.edu.hk (Y. Zhu).

https://doi.org/10.1016/j.jmst.2023.02.055
1005-0302/

The above theory provides insight into how hetero-deformation leads to superior strength-ductility synergy in HS materials. However, how hetero-deformation proceeds in reality to prevent the early failure caused by low strain hardening capability of hard zones is still not well understood. Recently, delocalization of strain bands (SBs) has been revealed as a unique deformation mechanism in HS materials, where dispersed SBs were nucleated at elastic-plastic deformation stage and propagated stably through the whole uniform elongation [11,24–26]. Wang and Huang et al. reported that the elastic/plastic interaction (coupling) between nano-grained layers and coarse-grained matrix promoted the formation of dispersed SBs in gradient Ni samples [25]. These are only preliminary observations of SBs, whose formation mechanism needs to be further probed to understand how the SB formation is related to GND pile-ups, strain gradients and mechanical behaviors.

In this work, we reveal the formation mechanism of dual-level hierarchical SBs in a HS Fe-40Cu model material. The mechanical behavior of the HS sample is related to the SB formation and effect of strain hardening capacity of soft copper zones. It is found that dispersed microscale strain bands (μSBs) with width of several micrometers were formed and propagated steadily during tensile deformation. These μSBs grouped together to form macroscale SBs uniformly over the entire gage section, accommodating the majority of the applied strain and raising the ductility of HS Fe-40Cu samples. The propagation of μSBs created high strain gradient within them, which was accommodated by GND accumulation.

2. Experiment

Pure iron powder (60 vol.%) was mixed with pure copper powder (40 vol.%) in a stainless steel vial. Stainless steel balls were loaded with a 2:1 balls to powder weight ratio. The Fe-40Cu powder mixture was sintered through hot rolling sintering (HRS): the powder mixture was first vacuum-sealed in 304 stainless steel pipes (outside diameter of 58 mm, wall thickness of 2 mm and length of 300 mm) under approximately 5 $\times 10^{-3}$ Pa. The sealed capsules were heated up to 1000 °C with a heating rate of 6 °C/min and pre-sintered for 1 h. Then HRS was performed with 4 passes at 1000 °C to roll the capsules to a final thickness of 10 mm. The as-HRS-processed capsules were cooled in air and the outer peel was removed by machining to obtain the final Fe-40Cu samples with dimensions of approximately 70 mm in width and 6 mm in thickness. The Fe-40Cu sheets were cold rolled from 6 mm to 1.2 mm (80% thickness reduction). Subsequently, a series of low-temperature annealing treatments, 320 °C for 0.5 h, 1 h, 3 h and 400 °C for 3 h, were conducted for heterostructuring, where iron matrix maintained hard and highly work hardened, while copper zones got progressively softened by recrystallization. The low annealing temperature was chosen far below the recrystallization temperature of iron so that the microstructures and tensile performance of the hard iron matrices remained almost unchanged after the annealing treatments.

Microstructures were characterized by optical microscopy (OM), scanning electron microscopy (SEM), transmission electron microscopy (TEM) and scanning transmission electron microscopy (STEM). Samples for electron backscattered diffraction (EBSD) and in-situ tensile tests under EBSD were first mechanically grinded and polished to achieve mirror-like surfaces and then ion-milled at 6 kV for 20 min to remove residual strain in the surface layer. The EBSD step size (l) was 0.1 μm to reveal detailed dislocation structure in iron matrix which possessed ultrafine subgrains and dislocation cells. The angular resolution of EBSD scanning is less than 0.05° TEM foils were prepared by first mechanically grinding down to about 40 μm and then ion-polishing with a polishing angle of 3°, at 4 kV and -60 °C, until a hole was observed.

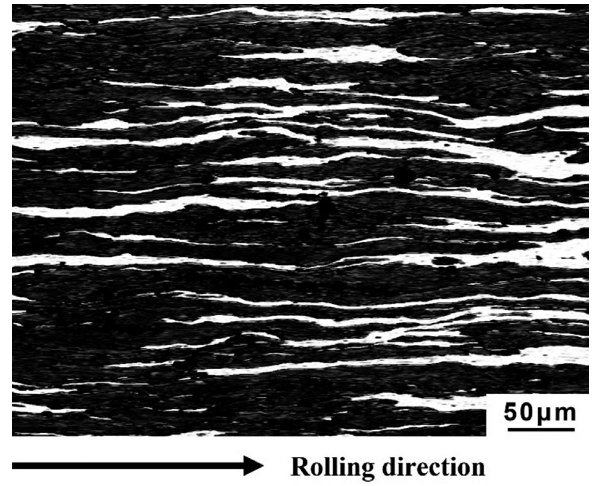

Fig. 1. A backscattered electron image shows the distribution of copper zones (white) and iron matrix (black) on the lateral surface of Fe-40Cu sheets after cold rolling.

TEM and STEM observation was performed with a JEM-2010F microscope (equipped with EDS detector) operating at 200 kV.

Micro-hardness tests were performed in a HVS1000A-XYT instrument with a load of 10 g held for 10 s. Dog-bone-shaped tensile samples with gage dimensions of 16 $\times$ 2 $\times$ 1.2 mm^3 were tested under uniaxial tension and loading-unloading-reloading (LUR) tension at a strain rate of 5 $\times 10^{-4}$ s^{-1} at room temperature. The uniaxial tensile tests and loading-unloading-reloading tests were repeated at least 3 times for each type of samples. Samples for in-situ tensile tests were first cut with gage dimensions of 3 $\times$ 0.45 $\times$ 1 mm^3. The testing surface was parallel with the side surface of the cold-rolled sheet and was prepared with the same procedure as the ones for EBSD samples. To avoid the blurring effect of artificial speckle patterns on the metallography and to build a direct correlation between strain maps and phase distribution maps, the morphology of the Fe-40Cu samples after etching was used as the speckle pattern for digital image correlation (DIC) analysis. The surface was first mechanically polished and then was etched with 4% nital solution for 5–10 s and with a mixture of deionized water (25 ml), ammonia (25 ml) and 3% hydrogen peroxide solution (5 ml) for 10–20 s separately. Similar etching methods have been used to produce speckle patterns for DIC analysis in various metals and alloys [24,27–29]. The in-situ tensile tests under EBSD were conducted at a rate of 0.03 mm/min in a GeminiSEM 300 instrument equipped with a GATAN MTEST2000 uniaxial testing stage. The strain distribution and evolution on the lateral surface of the Fe-40Cu sheets were recorded by in-situ tensile tests under SEM. To avoid the haze induced by artificial microscale speckle patterns on the metallographic analysis during tensile deformation, the morphology of the heterostructures was used as speckle patterns for DIC analysis. DIC program (Ncorr v1.2) was used to analyze relative displacements of the successive images with respect to the reference image [30]. The calculation step was 2 pixels; the radius of the subset was 36 pixels; and the radius of strain calculation window was 15 pixels.

3. Results

3.1. Structural characterization

The macroscale distribution of copper zones on the lateral surface after cold rolling is characterized by backscattered electron imaging (Fig. 1). The original copper powder or clusters were significantly elongated along the rolling direction after HRS

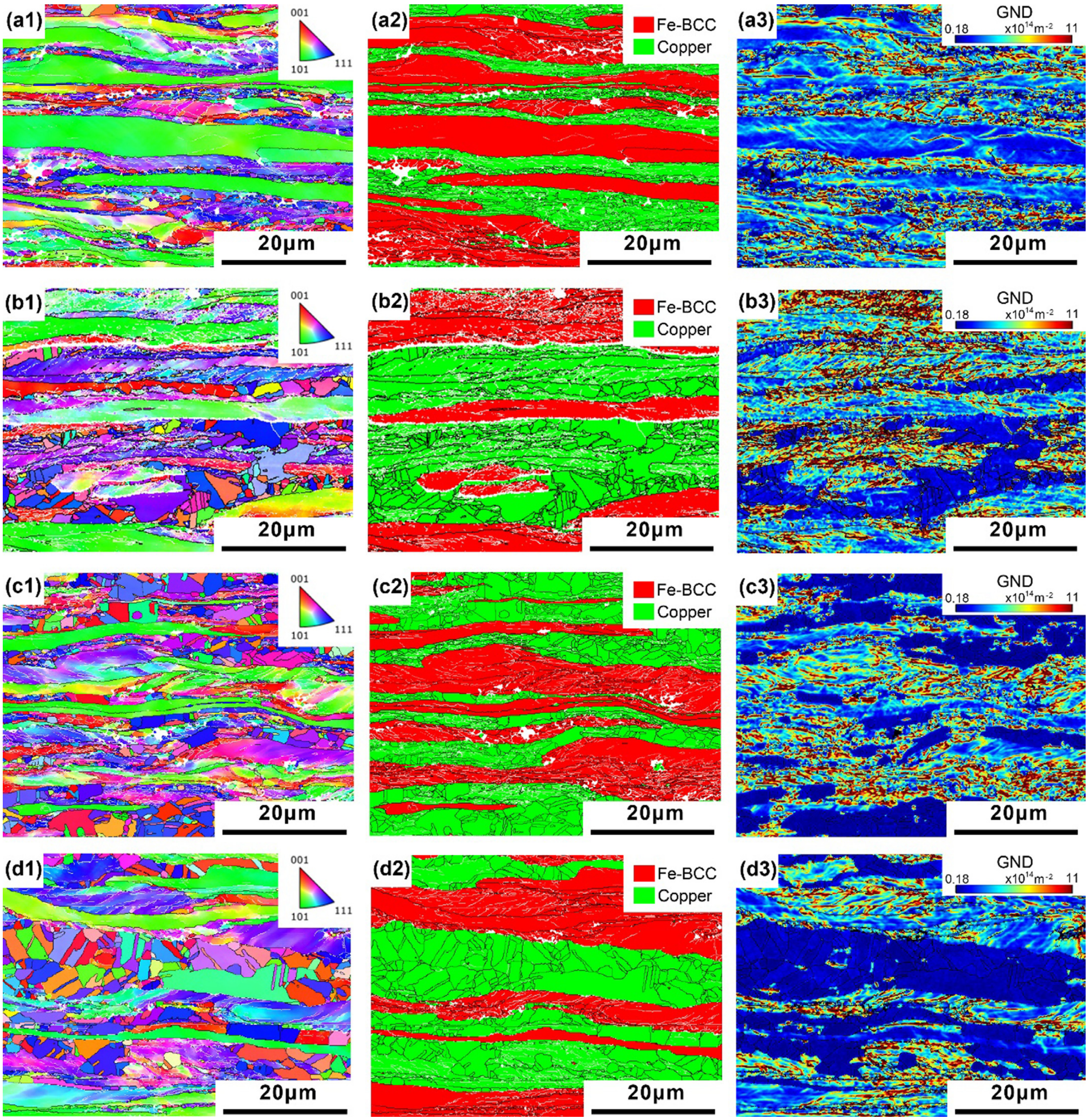

Fig. 2. Typical IPF maps, phase maps and cold-rolling-induced GND distribution maps of Fe-40Cu samples after annealing at 320 °C for 0.5 h (a), at 320 °C for 1 h (b), at 320 °C for 3 h (c) and at 400 °C for 3 h (d).

and cold rolling, forming copper lamella embedded in the iron matrix.

The typical inverse pole figure (IPF) images, phase morphologies and GND distribution maps are shown in Fig. 2. The GND density (ρ_{GND}) is calculated based on the Nye tensor [31–33], which contains lattice curvature tensor components. The Nye tensor was extracted from the EBSD data using an open-source analysis software (ATEX) [34]. A misorientation threshold of 10° was applied to exclude the effect of any misorientation caused by grain boundaries on ρ_{GND}. Different values of pixel separation distance ($\Delta x = l$, $2l$ and $3l$, $l = 100$ nm) were first tested in calculation of ρ_{GND} and 200 nm was verified to be reasonable. Because it not only provided good spatial resolution of ρ_{GND} characterization in iron matrix with ultrafine subgrains, but resulted in a reasonable noise and spread of ρ_{GND} [31,35]. The noise floor of GND density ($\Delta\rho_{\mathrm{GND}}$) was estimated to be around 8.7×10^{12} m^{-2} according to the equation: $\Delta\rho_{\mathrm{GND}} = \delta/b\Delta x$ [36], where δ is the angular resolution (0.05°, upper-bound) and b is the norm of Burgers vector. ρ_{GND} less than the noise floor was excluded and the discrete ρ_{GND} data was fitted with a lognormal probability function for each sample to

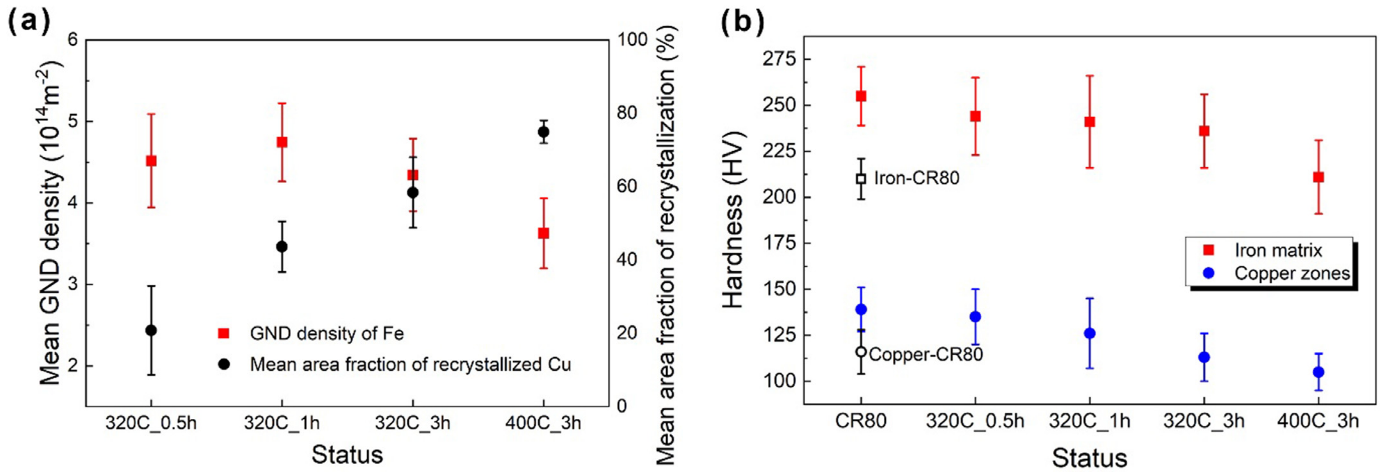

Fig. 3. (a) The evolution of mean density of cold-rolling-induced GNDs in iron matrix as well as mean area fraction of recrystallized copper grains after various annealing treatments. (b) The evolution of hardness of iron matrix and copper zones before and after these annealing treatments. The hardness of cold-rolled pure iron counterparts (Iron-CR80) and pure copper counterparts (Copper-CR80) is also shown in (b). The error bars indicate the standard deviation of the statistics.

achieve the microstructure-averaged value of $\rho_{\rm GND}$ [31,32]. Note that the GNDs calculated here (Fig. 2) are induced not by hetero-deformation but by residual strain produced by cold rolling. Therefore, here these GNDs are called cold-rolling-induced GNDs and are considered as residual dislocation structures. In the IPF images and phase maps, grain boundaries (GBs) with misorientation angles above 10° are depicted with black lines and those with misorientation angles in range of 3°−10°, which are mostly subgrain boundaries and dense dislocation walls, are depicted with white lines. As shown in Fig. 2(a1) and (a3), both iron and copper grains were severely elongated after cold rolling with dense residual dislocation structures. Annealing at 320 °C brought negligible microstructural change in the iron matrix, where iron grains stayed elongated and maintained high density of cold-rolling-induced GNDs. In contrast, copper zones were progressively recrystallized during annealing at 320 °C. Equiaxial recrystallized copper grains with low density of cold-rolling-induced GNDs accounted for larger area with further annealing at 320 °C. Raising the annealing temperature to 400 °C facilitated the recovery of deformation-induced dislocation structures and further improved the recrystallization of deformed copper grains.

The statistical results of mean densities of cold-rolling-induced GNDs in the iron matrix and recrystallized copper grains are shown in Fig. 3(a), in which each data is obtained by averaging values of five EBSD scanning results for each annealing treatment. The recrystallized grains are determined as grains with grain orientation spread (GOS) value extracted from EBSD data less than 3°. The mean density of cold-rolling-induced GNDs in the iron matrix stayed high during annealing at 320 °C and only slightly dropped to 3.6 $\times 10^{14}$ m^{-2} due to recovery after annealing at 400 °C for 3 h. Meanwhile, the mean area fraction of recrystallized grains in copper zones increased from 21% to 75%. This means that the strain hardening capacity of copper zones was progressively increased, as the residual dislocation structures were diminished by recovery and recrystallization. In Fig. 3(b), the hardness evolution of iron matrices is consistent with that of their mean cold-rolling-induced GND densities with an obvious drop after annealing at 400 °C for 3 h. Besides, the hardness gap between iron matrix and copper zones indicates strong heterogeneity in strength in all HS_Fe-40Cu samples, which is critical for hetero-deformation.

Fig. 4 shows the intragranular microstructures of iron matrix and copper zones after annealing. Typical deformation-induced dislocation walls and subgrain boundaries subdivide large elongated iron grains into ultrafine dislocation cells and subgrains in Fe-40Cu-320C_1 h and Fe-40Cu-320C_3 h samples. A large amount of residual dislocation entanglements remained in these ultrafine substructures with the help of dispersed copper precipitates. This explains why the iron matrix with large elongated grains possessed high strength and low ductility. Fig. 4(c) shows that the dense dislocation entanglements in iron grains were obviously removed by recovery after annealing at 400 °C for 3 h. As a result, the hardness of iron matrix dropped obviously from 236 HV (320C_3 h) to 211 HV, as shown in Fig. 3(b). Typical microstructures in recrystallized copper grains are shown in Fig. 4(d), where the density of residual dislocations was pretty low and annealing twins grew from the Fe-Cu interface. Some residual dislocation entanglements were left due to the pinning effect of spherical iron precipitates. The formation of iron precipitates and copper ones was attributed to the Fe-Cu mutual diffusion during sintering. And some large copper precipitates were elongated together with the matrix during cold rolling, as they were softer than the surrounding iron matrix, as marked by white arrows in Fig. 4(a–c). The extra strengthening caused by these precipitates raised the strength of cold rolled Fe-40Cu samples (Fe-40Cu-CR80) higher than that of their pure iron counterparts (Iron-CR80), as shown in Fig. 5(a), and was estimated by hardness gap between iron matrix and pure iron counterparts and that between copper zones and pure copper counterparts after cold rolling, which were about 45 HV for iron and 23 HV for copper (Fig. 3(b)).

3.2. Mechanical properties

Fig. 5 presents the tensile behavior of HS Fe-40Cu samples and the pure iron, which was used to approximate the tensile performance of free-standing iron matrices. The HS Fe-40Cu samples present better strength-ductility combination than the pure iron. The Fe-40Cu-CR80 samples possess an ultimate tensile strength (UTS) of 687 MPa, which is much higher than that (566 MPa) of the Iron-CR80 samples. This strength gap is mainly attributed to the extra strengthening caused by iron-copper mutual diffusion, including precipitation strengthening, solid solution strengthening and extra dislocation accumulation with the pinning effect of the precipitates.

In Fig. 5(a), annealing at 320 °C barely changed the tensile performance of pure iron with their yield strength staying around 525 MPa-535 MPa and their uniform elongation remaining less

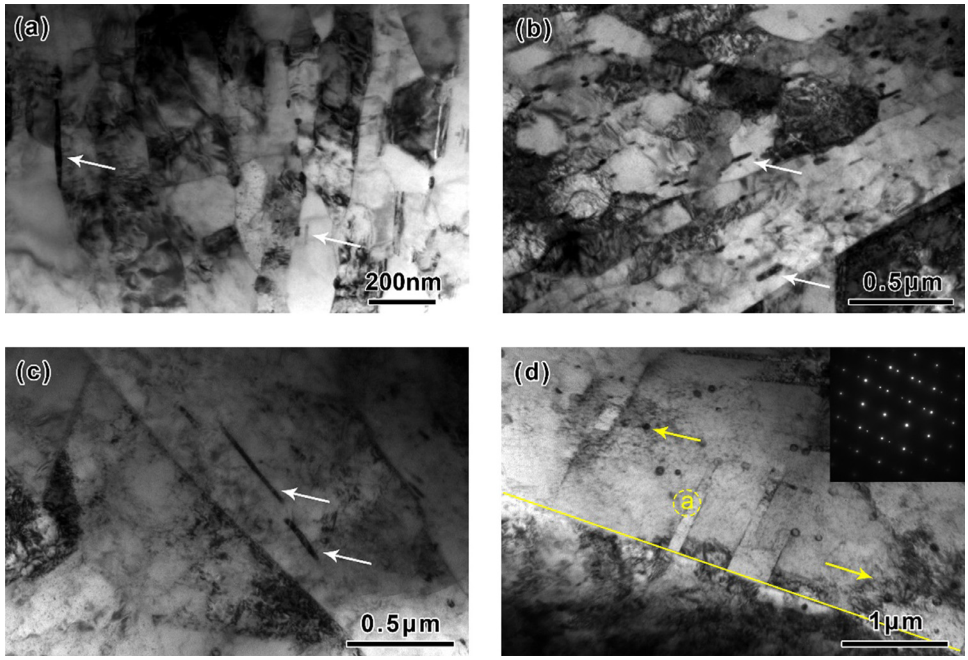

Fig. 4. TEM images showing typical microstructures in the iron matrix in Fe-40Cu-320C_1 h (a), Fe-40Cu-320C_3 h (b) and Fe-40Cu-400C_3 h (c) samples. Nanosized copper precipitates are marked by white arrows. (d) Typical microstructures in recrystallized copper grains in a Fe-40Cu-320C_3 h sample. The inset is a selected area diffraction pattern taken at spot "a" that reveals an annealing twin growing from the Fe-Cu interface (marked by a yellow line) and nanosized iron precipitates are marked by yellow arrows.

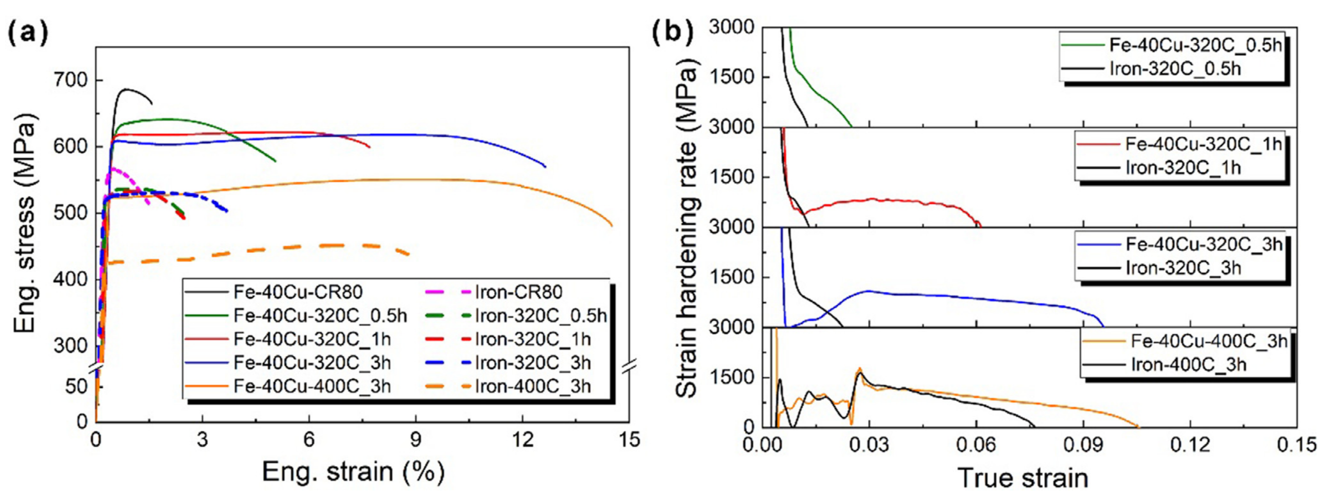

Fig. 5. (a) Engineering strain-stress curves of HS Fe-40Cu samples and the pure iron and (b) their strain hardening rate-true strain curves.

than 1.7%. In contrast, the uniform elongation of HS Fe-40Cu samples was considerably improved during heterostructuring at 320 °C from 2.0% (Fe-40Cu-320C_0.5 h) to 8.1% (Fe-40Cu-320C_3 h) only at a low cost of yield strength of 23 MPa. This is primarily attributed to the hetero-deformation induced (HDI) hardening and new deformation mechanism induced by the hard iron-soft copper heterostructure, which will be discussed later. Interestingly, annealing at 400 °C for 3 h, which further released the strain hardening capacity of copper zones, did not improve the uniform elongation of the Fe-40Cu-400C_3 h samples much but led to a considerable drop in yield strength from 609 MPa to 522 MPa due to recovery-induced softening of the hard iron matrix.

The strain hardening rate-strain curves are shown in Fig. 5(b), which indicate that HDI hardening contributed to the total strain hardening rate of HS Fe-40Cu samples ($\theta_{Fe-40Cu}$). In Fe-40Cu-320C_0.5 h samples, as the strain hardening capacity of the copper zones was low, HDI hardening was depressed and only slowed down the drop of the total strain hardening rate of Fe-40Cu-320C_0.5 h samples to some extent. In Fe-40Cu-320C_1 h and Fe-40Cu-320C_3 h samples, as the strain hardening capacity of the copper zones was progressively restored, an up-turn of $\theta_{Fe-40Cu}$ appeared at the early stage of plastic deformation, implying strong HDI hardening [37,38]. In Fe-40Cu-400C_3 h samples, in addition to the strain hardening capacity of the soft copper zones being further increased, the hard iron matrix was softened due to recovery and its strain hardening capacity and plastic deformability were consequently restored. The $\theta_{Fe-40Cu}$ of Fe-40Cu-400C_3 h sample shows an extended plateau similar to that of the Iron-400C_3 h

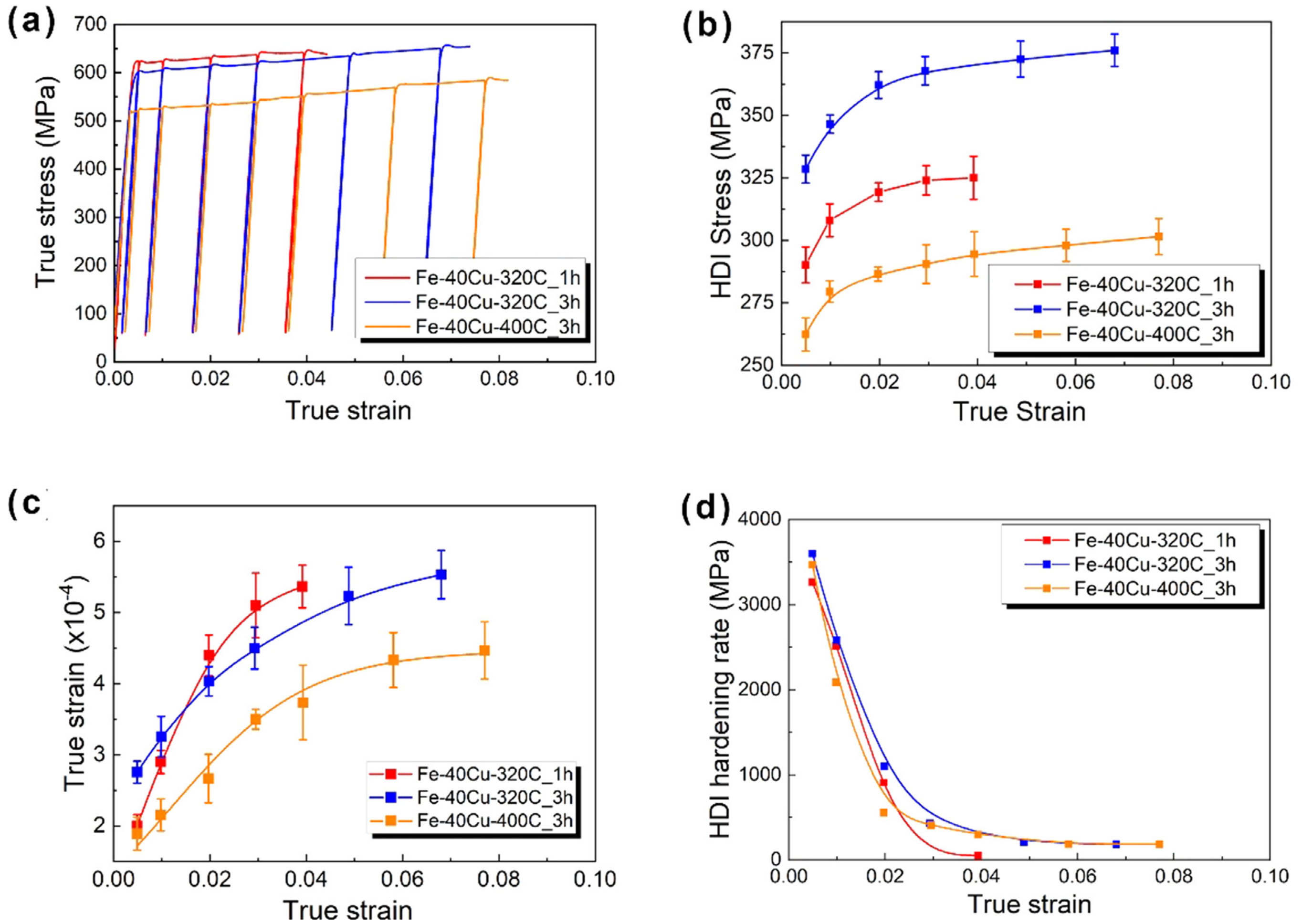

Fig. 6. (a) The loading-unloading-reloading curves of three HS Fe-40Cu samples; The evolution of hetero-deformation induced stress (b), anelastic strain (c) and hetero-deformation induced hardening (d) during tensile deformation.

counterparts, implying that the strain hardening of the hard iron matrix dominated the $\theta_{Fe-40Cu}$ at the early stage of plastic deformation. HDI hardening increased with plastic deformation and helped with sustaining high total strain hardening at higher applied strain. However, comparing the $\theta_{Fe-40Cu}$ of Fe-40Cu-400C_3 h with that of Fe-40Cu-320C_3 h, the total strain hardening at high strain level was not obviously improved by further raising the strain hardening capacity of the soft copper zones.

4. Discussion

4.1. HDI stress and hardening

Loading-unloading-reloading (LUR) tensile tests were conducted to reveal HDI stresses in HS Fe-40Cu materials. Typical LUR hysteresis loops of the HS Fe-40Cu samples are shown in Fig. 6(a). HDI stress (σ_{HDI}) is calculated using the equation [39]:

$$\sigma_{HDI} = \frac{\sigma_u + \sigma_r}{2} \tag{1}$$

where σ_u and σ_r are unloading and reloading yield stresses, respectively. In this study, the unloading and reloading yield points are defined as points where the slope ($\Delta\sigma_{true}/\Delta\varepsilon_{true}$) deviates 5% from the effective Young's modulus (E_{eff}), which is the slope of the linear part in unloading and reloading cycles. [39]

As shown in Fig. 6(b), when the hard iron matrix stayed strong with low plasticity, σ_{HDI} increased with increasing the strain hardening capacity of soft copper zones by further annealing at 320 °C from 1 h to 3 h. The σ_{HDI} strengthened the copper zones and lowered the strength cost of the HS Fe-40Cu materials for improving the ductility. The σ_{HDI} dropped considerably in Fe-40Cu-400C_3 h samples, which is primarily attributed to the hard iron matrix being softened by recovery at 400 °C. Besides, the HDI stresses of these heterostructured Fe-40Cu samples accounted for more than half of the applied stresses, implying considerable anelasticity during the unloading-reloading cycles. Therefore, anelastic strain is also presented here to verify the trend of the HDI stress, as shown in Fig. 6(c). The anelastic strain was estimated based on the equation: $\varepsilon_a = \varepsilon_r - \Delta\sigma/E$ [40], where ε_a is the anelastic strain, ε_r is the recoverable strain, $\Delta\sigma$ is the stress drop of the unloading section and E is the physically-measured Young's modulus. The evolution of the anelastic strain shows a similar trend to that of the HDI stress, as they both grow fast at the early stage of plastic deformation and their growth considerably slows down at high strain levels. But it should be noted that the growth of the HDI stress is not identical to that of the anelastic strain, especially at the low plastic strain level, which needs further study.

The HDI hardening is defined as,

$$\theta_{HDI} = \frac{d\sigma_{HDI}}{d\varepsilon} \tag{2}$$

Fig. 6(d) shows that the HDI hardening in the Fe-40Cu-320C_1 h sample dropped rapidly with applied strain due to low

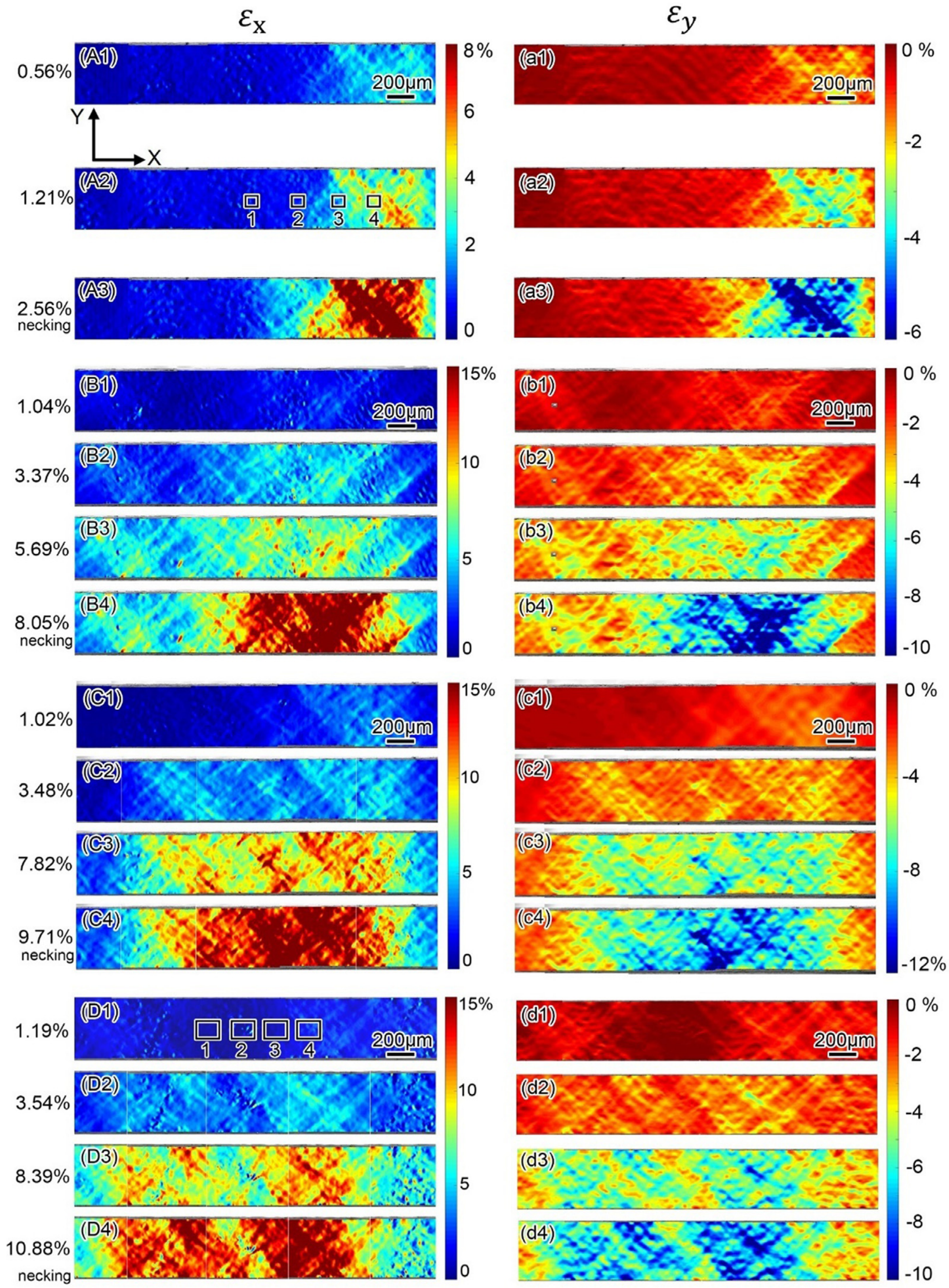

Fig. 7. Strain maps at a low magnification in the tensile loading direction (left column) and in the sample thickness direction (right column) in (A, a) a Fe-40Cu-CR80 sample, (B, b) a Fe-40Cu-320C_1 h sample, (C, c) a Fe-40Cu-320C_3 h sample and (D, d) a Fe-40Cu-400C_3 h sample. The *X* axis and *Y* axis represent the tensile loading direction and the sample thickness direction respectively. The percentage on the left side of each subgraph represents the applied strain point where the μ-DIC was performed and the percentage with "necking" under it means that the strain point was in necking zones.

strain hardening capacity in the soft copper zones. Note that the HDI hardening comes mostly from the back stress hardening in the soft zones. Copper has medium stacking fault energy and tends to form dislocation cell structure instead of planar slip, which makes it not very effective in developing GND pile-ups and back stress [41]. The copper zones with low strain hardening capacity provided weak constraint to the local strain localization, resulting in fast development of catastrophic strain accumulation zone and unsustainable hetero-deformation. This will be further discussed in Section 4.2.

With more strain hardening capacity being released in the Fe-40Cu-320C_3 h sample, the HDI hardening became sustained to produce high uniform elongation. After annealing at 400 °C for 3 h, the hard iron matrix was softened by recovery to regain plastic deformability to some extent. This results in relatively weaker strain partitioning between iron matrix and copper zones and lower HDI

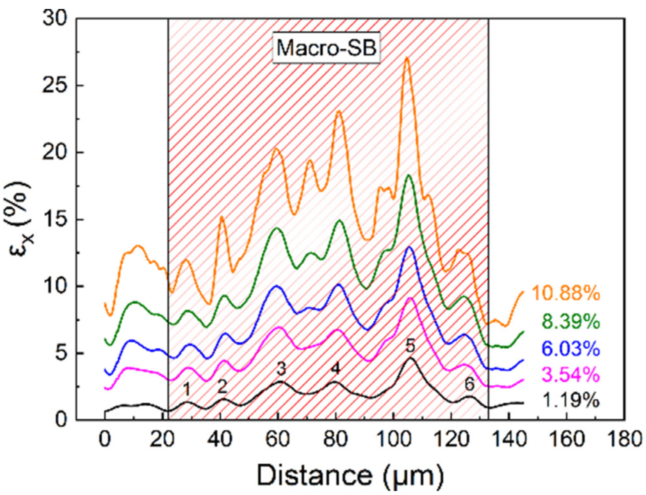

Fig. 8. The ε_x profiles at various strain levels of μSBs in a macro-SB in the Fe-40Cu-400C_3 h samples. The red rectangular shadow represents the macro-SB.

hardening at the early stage of deformation. As shown in Fig. 6(d), the HDI hardening of the Fe-40Cu-400C_3 h samples is obviously lower than that of the Fe-40Cu-320C_3 h sample before the applied strain reaches 4%. This is consistent with the $\theta_{\text{Fe}-40\text{Cu}}$-strain behavior shown in Fig. 5(b). Besides, compared with the HDI hardening rate in the Fe-40Cu-320C_3 h samples, the additional 17% recrystallized copper grains in the Fe-40Cu-400C_3 h samples did not produce much improvement to HDI hardening at high plastic strain level. This implies that another factor is also affecting the efficiency of strain hardening capacity of soft copper zones.

4.2. Evolution of strain bands with strain hardening capacity

In-situ tensile tests under SEM and EBSD were conducted to analyze strain distribution and to characterize GND accumulation with applied strain. It should be noted that the KAM method cannot reveal the tensor nature of GNDs. Nevertheless, it can still be used to estimate the GND density distribution [42].

Strain maps of Fe-40Cu samples after cold rolling and various annealing treatments are shown in Fig. 7, where ε_x is the strain in the tensile loading direction and ε_y is the strain in the sample thickness direction. We define the local branch-like SBs shown in Fig. 7 as the macroscale strain bands (macro-SBs), because of their large sizes (35–72 μm in width and tens to a few hundreds of microns in length). In Fig. 7(A, a), early macro-SBs developed fast into a large strain accumulation zone soon after yielding in the Fe-40Cu-CR80 sample. The rapid growth of the strain accumulation zone left no chance for the rest of the gage section to accumulate plastic strain and caused early fracture. In contrast, macro-SBs were uniformly distributed along the gage section in the Fe-40Cu-320C_3 h and Fe-40Cu-400C_3 h samples, accommodating the majority of the applied strain and delaying the development of catastrophic strain localization, see Fig. 7(C, c) and (D, d). These two distinct types of deformation behavior are resulted from the difference in stability of macro-SBs, which should be related to the synergistic deformation between iron matrix and copper zones and was enhanced by increasing the strain hardening capacity of copper zones.

4.3. Hierarchical strain bands

The macro-SBs are macroscopic strain distribution phenomenon, while the interaction between iron matrix and copper zones during deformation is at microscale. Therefore, to figure out the reasons for the transition from unstable macro-SBs to stable macro-SBs, high-magnification DIC was conducted to unveil details of the development of macro-SBs. Figs. 9 and 10 present the high-magnification distribution and evolution of ε_x in the sites marked by “1 to 4″ in Fig. 7(A2) and (D1). It was found that the macro-SBs were composed of smaller μSBs. Dense μSBs with width of 5–8 μm grew within the macro-SBs, extending at angles of 37°−50° to the tensile direction. The inhomogeneous growth and grouping of the μSBs led to the formation of macro-SBs, where μSBs are stronger and/or denser. Fig. 8 shows the ε_x profile across a group of μSBs (marked by “1 to 6″) that together formed a macro-SB in the Fe-40Cu-400C_3 h sample. These μSBs did not grow uniformly with the applied strain, but instead the μSBs in the middle (3, 4, 5) rose much faster than the other three. A new strain peak showed up between μSB 3 and μSB 4 during deformation, as a weak μSB grew rapidly and caught up with them. These fast-growing μSBs raised the local strain level within the macro-SB, which at a low magnification level appears as the growth of the macro-SB.

Therefore, the stability of macro-SBs depends on the evolution of μSBs. As shown in Fig. 9, the early-developed μSBs in the Fe-40Cu-CR80 sample grew rapidly with the applied strain. Dramatic strain accumulated within these μSBs, accelerating their growth and the formation of a predominant strain localization zone. This hindered the formation and growth of μSBs away from the strain localization zone and left no chance for the rest of the gage section to accommodate plastic strain. In contrast, the strain localization in the Fe-40Cu-320C_3 h and Fe-40Cu-400C_3 h samples was constrained and the growth of early-developed μSBs was stabilized. As seen in Fig. 10, the μSBs appeared in the site 4 of the Fe-40Cu-400C_3 h sample are regarded as early developed μSBs, as they are much stronger than those in the other three areas. Unlike the early developed μSBs in the Fe-40Cu-CR80 sample, they grew stably with subsequently formed μSBs in the other three areas. Macro-SBs consequently got a chance to form uniformly along the gage section to accommodate the majority of applied strain. This unique strain accommodating mechanism has also been reported in other HS materials [11,25,27,43].

To quantitively characterize the development of μSBs, profiles of strain in the tensile direction (ε_x) across μSBs in different HS Fe-40Cu samples are extracted from their strain maps. Typical ε_x strain peaks at different strain levels are shown in Fig. 11(a–d). Fig. 11(e) demonstrates how integrated strain intensity (I_{int}) and full width at half maximum (W) of ε_x peak profiles are extracted by Gaussian fitting. The statistical results are plotted in Fig. 11(f), where each data point was averaged from the values of 5 randomly selected μSBs. The ε_x strain peaks indicate that μSBs accommodated more strain than that in the non-strain banding zones. The $\bar{I}_{\text{int}}$ of μSBs in Fe-40Cu-CR80 samples increased rapidly with the applied strain, while both $\bar{I}_{\text{int}}$ and the slope of $\bar{I}_{\text{int}}$ vs applied strain curves were progressively reduced after the low-temperature annealing treatments. This indicates that the growth of μSBs was stabilized in the annealed HS Fe-40Cu samples. The $\bar{W}$ barely changed with increasing applied strain, indicating that μSBs did not expand transversely during plastic deformation.

4.4. Stabilization of μSB propagation

The stability of μSBs primarily depends on GND accumulation in the copper zones. Fig. 12 depicts strain maps of ε_x in a Fe-40Cu-400C_3 h sample at high magnification. The Fe-Cu interfaces are outlined by black dashed lines and the iron zones are marked by “Fe” on the right. Abundant sites that were vulnerable to stress concentration were introduced by the random distribution of copper zones and inhomogeneous strain accumulation in hard iron

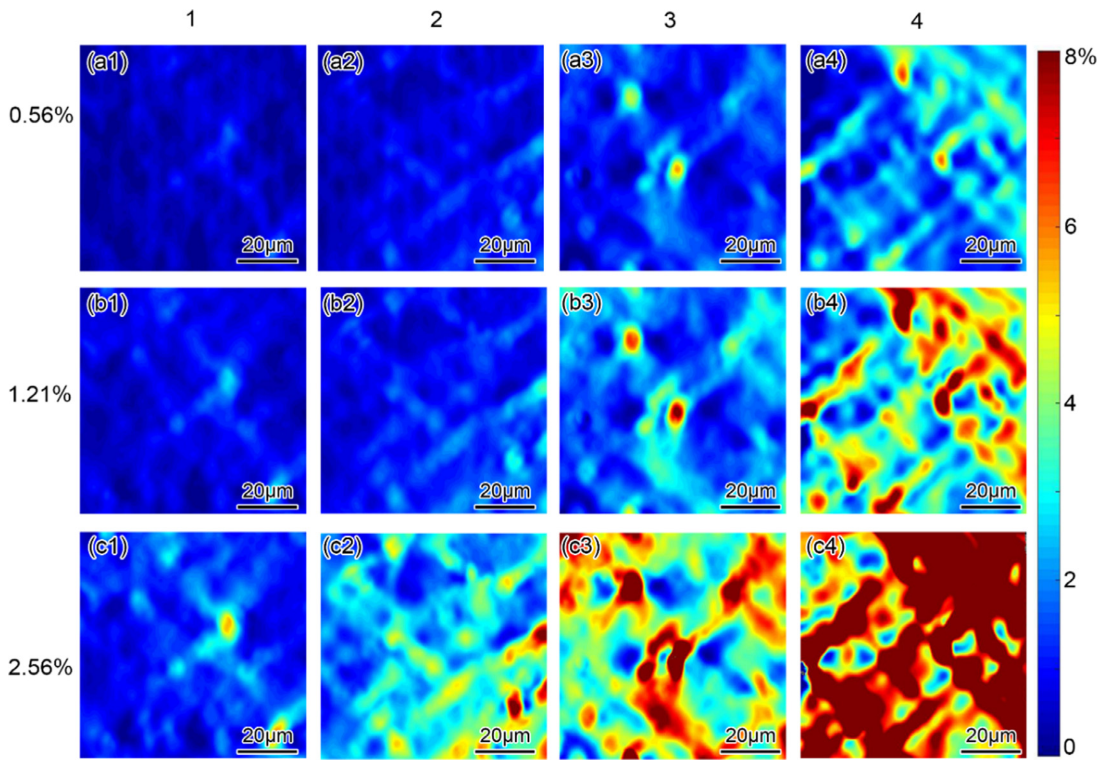

Fig. 9. High magnification strain (ε_x) distribution maps of the sites marked by "1, 2, 3, 4″ in Fig. 7(A2). Each column of subgraphs shows the evolution of μSBs in each site.

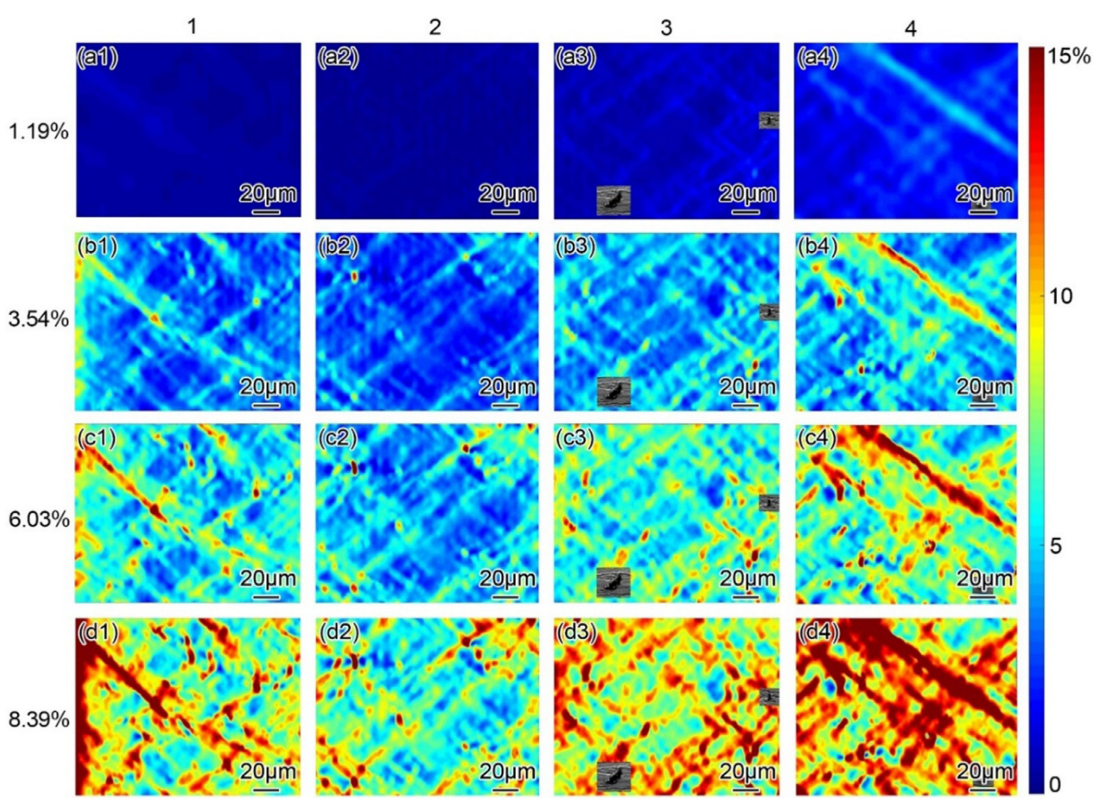

Fig. 10. High magnification strain (ε_x) distribution maps of the sites marked by "1, 2, 3, 4″ in Fig. 7(D1). Each column of subgraphs shows the evolution of μSBs in each site.

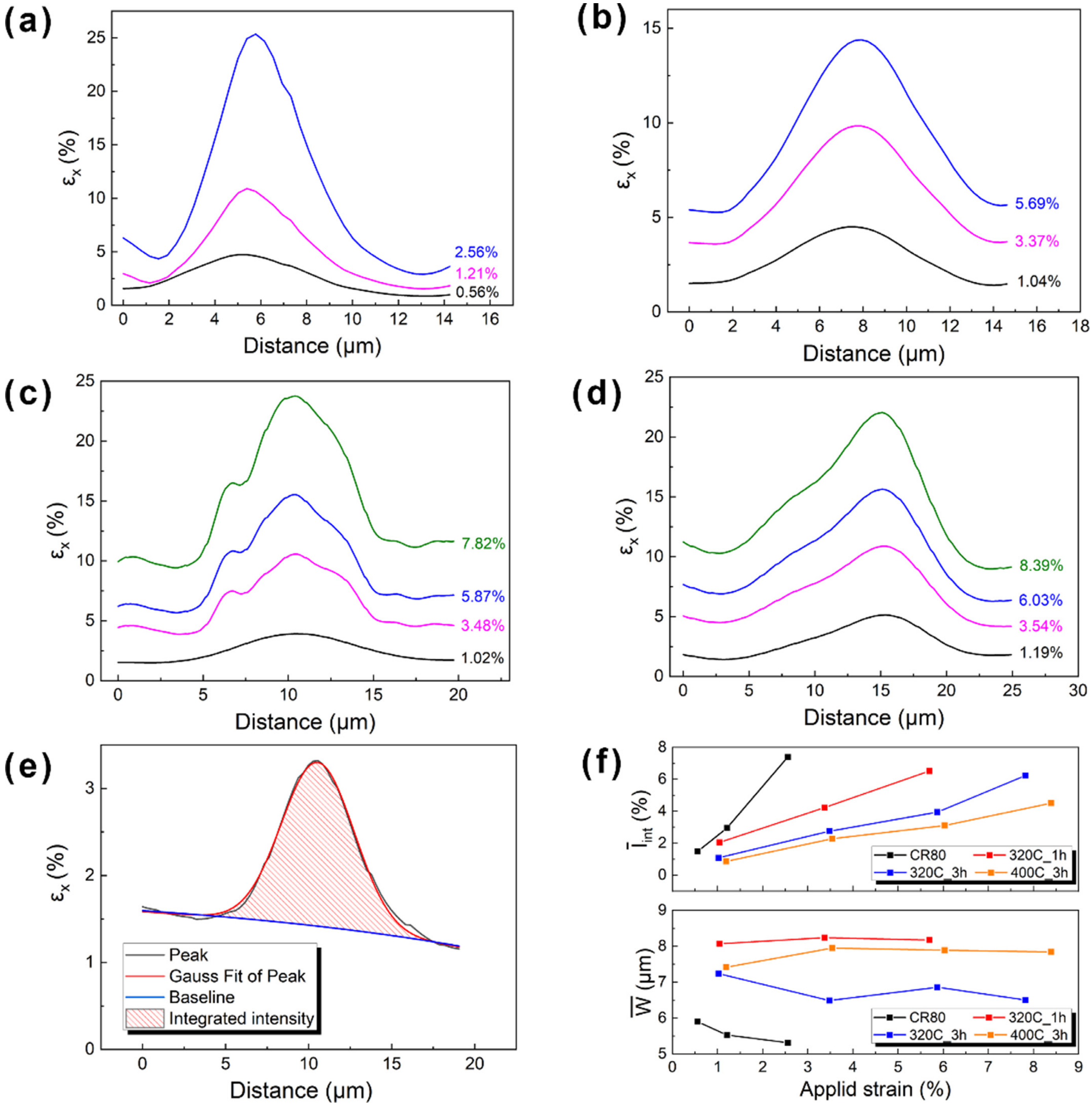

Fig. 11. Profiles of ε_x across representative μSBs in (a) a Fe-40Cu-CR80 sample, (b) a Fe-40Cu-320C_1 h sample, (c) a Fe-40Cu-320C_3 h sample and (d) a Fe-40Cu-400C_3 h sample. (e) Schematic image of how integrated strain intensity (I_{int}) and full width at half maximum (W) are extracted from the ε_x peak profiles. (f) The evolution of $\bar{I}_{\text{int}}$ and $\bar{W}$ with increasing the applied strain.

matrix during cold rolling. These sites are believed to be potential sites for μSB nucleation [24,44,45]. The μSBs were constrained by the surrounding copper zones, which prevented them from developing into catastrophic failure sites. With increasing applied strain, the μSBs grew as the localized strain in the iron sections of the μSBs rose significantly, as shown in the red shadowed area in Fig. 12(b–d), and transmitted into surrounding copper zones at angles of 37°–50° to the tensile direction. High strain gradient was generated in the μSBs by the strain transmission. As shown in Fig. 12(b–d), the longitudinal distribution profiles of ε_x along SBs marked by AB CD and EF in Fig. 12(a) present increasing strain gradients as the μSBs grew. The high strain gradient was primarily accommodated by GND accumulation in copper zones (Fig. 14). These GNDs in turn produced long-range back stress to hinder the strain flow and the propagation of existing μSBs, leaving opportunities for μSBs to form elsewhere. Therefore, GND accumulation in copper zones played an important role in stabilizing the growth of μSBs.

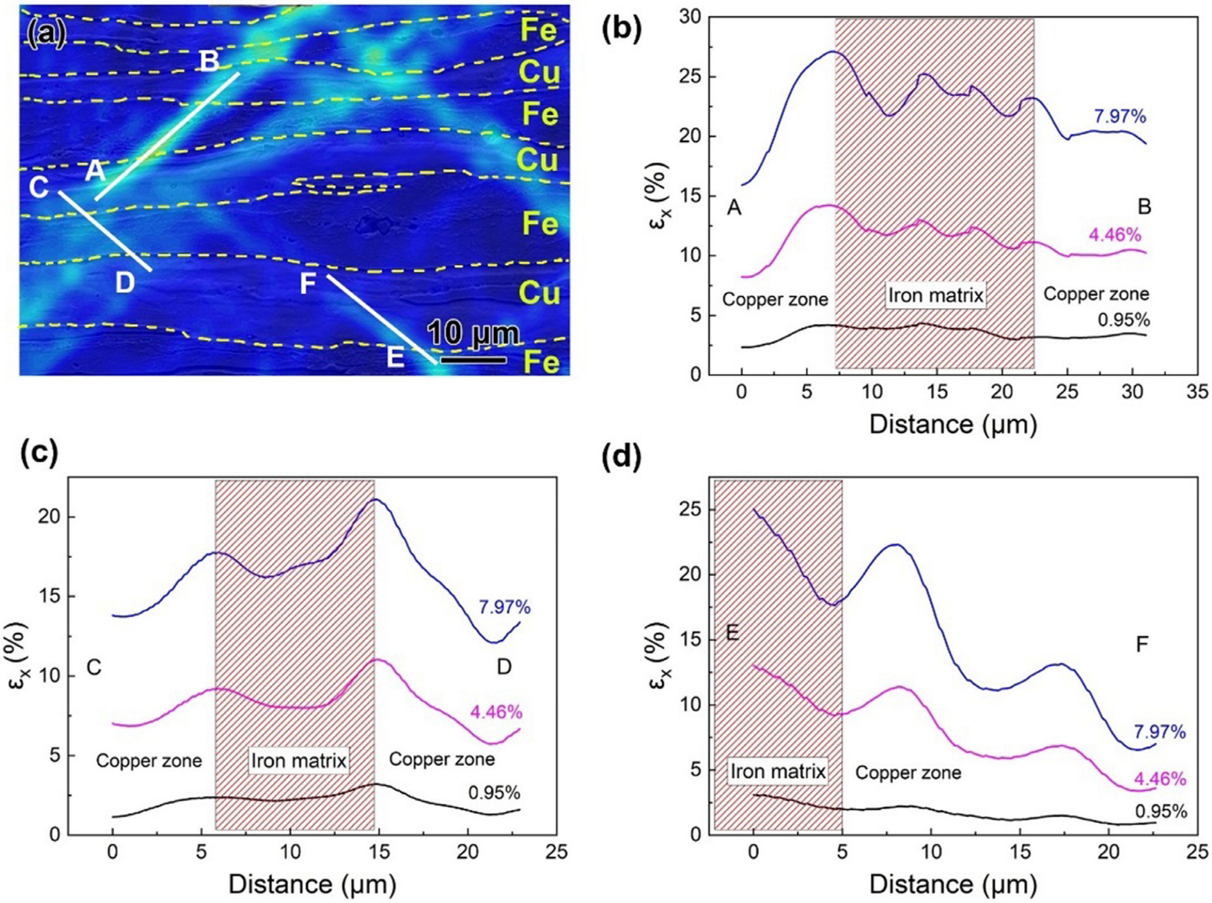

Fig. 12. (a) The strain map of ε_x (a) and profiles of ε_x along the longitudinal direction of three typical μSBs (b–d) in a Fe-40Cu-400C_3 h sample. The three typical μSBs are marked by "AB", "CD" and "EF" respectively. The Fe-Cu boundaries are outlined by yellow dashed lines and the iron matrix and copper zones are marked by "Fe" and "Cu" on the right. In (b–d), the iron matrix is referred as the red shadow area. And the percentages on the right of the strain profile curves are the applied strain where μ-DIC analysis was conducted.

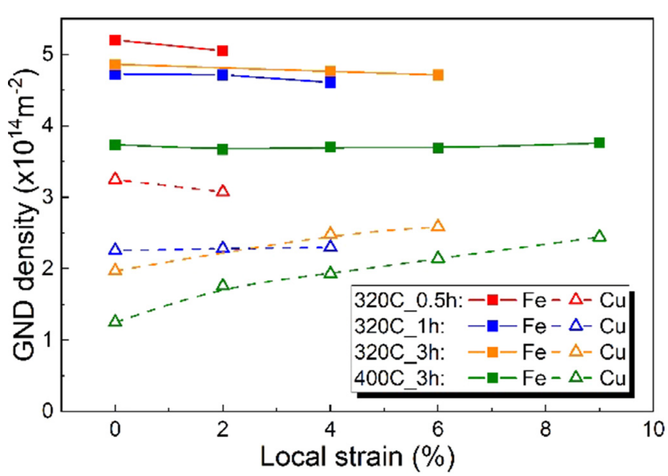

Fig. 13. The evolution of GND density with the applied strain in the HS Fe-40Cu samples.

Fig. 13 presents the evolution of GND density during plastic deformation. The GND density leveled off with the applied strain in the iron matrices of all four HS Fe-40Cu samples. This is because the iron matrices possessed little room for accumulating GNDs as they were still highly deformed with extremely low strain hardening capacity. In contrast, the accumulation of GNDs in the copper zones was progressively promoted, as the strain hardening capacity of the copper zones was restored by low-temperature annealing. Therefore, raising the strain hardening capacity of soft copper zones promoted the accumulation of GNDs and stabilized the development of μSBs.

Fig. 14 presents the evolution of GND accumulation in soft copper zones with the applied strain and the corresponding ε_x maps in the 400C_3 h sample. The iron matrix in GND distribution maps is whited out to make a clear contrast of GND accumulation in the soft copper zones at various strain points. These results reveal that GNDs primarily accumulated within the μSB areas during plastic deformation to accommodate the high strain gradient among the μSBs. This concentrated GND accumulation not only produced long-range back stress to hinder the propagation of μSBs, but served as barriers to further dislocation slip, resulting in stable μSB development and high strain hardening capability of HS Fe-40Cu samples.

It should be noted that as GNDs primarily accumulated within the μSBs in copper zones, the strain hardening capacity in the non-SB areas of copper zones was not sufficiently used and thus had limited contribution to the stabilization of μSBs and HDI hardening. This explains why the uniform elongation and strain hardening rate at high strain level of Fe-40Cu-400C_3 h samples were not significantly improved by further raising the strain hardening capacity of the copper zones, compared with those of Fe-40Cu-320C_3 h samples.

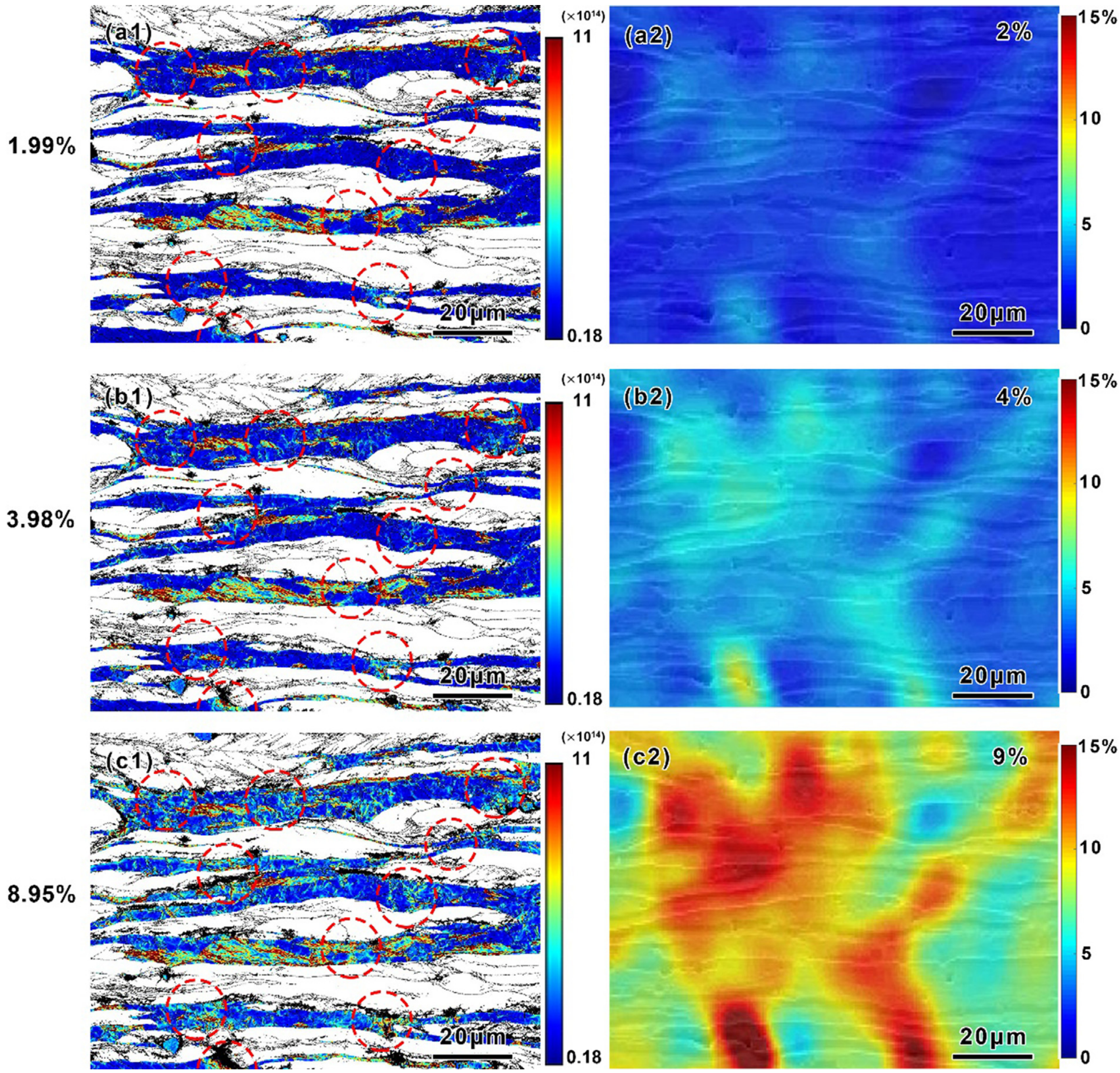

Fig. 14. The evolution of GND accumulation in copper zones (in the left column) and the corresponding ε_x distribution maps (in the right column) at varying strain points, 1.99%, 3.98% as well as 8.95%, in a Fe-40Cu-400C_3 h sample.

5. Conclusions

In this study, we designed a model heterostructured Fe-40Cu materials to study the dependence of tensile performance on deformation behavior. The development of hierarchical SBs was found to play a key role in improving the ductility of the heterostructured materials. The main conclusions are:

(1) The process of hetero-deformation in HS Fe-40Cu materials consists of formation and propagation of μSBs. The steady propagation of μSBs stabilized plastic deformation of the iron matrix and grouped together to form macro-SBs that are uniformly distributed over the gage section of the tensile samples so that the strain hardening capacity of the HS materials can be sufficiently utilized to increase the uniform elongation.

(2) As the μSBs grew, strain localized significantly in the iron matrix and transmitted into surrounding soft copper zones at angles ranging from 37° to 50° to the tensile direction. High strain gradient was generated by the strain transmission within the μSBs and was accommodated by GND accumulation, which in turn hindered propagation of the existing μSBs and provided an opportunity for growth of subsequently formed μSBs.

(3) Increasing strain hardening capacity of soft copper zones provided more room for GND accumulation and thus enhanced their constraint to the propagation of μSBs. Besides, GNDs were primarily accumulated within the μSBs in soft copper zones, suggesting that improving the spatial distribution and density of μSBs in the copper zones should further improve the stability of μSBs and the ductility of heterostructured materials.

Declaration of Competing Interest

The authors declare that they have no known competing financial interests or personal relationships that could have appeared to influence the work reported in this paper.

Acknowledgments

Y.T. Zhu acknowledges the support of the National Key R&D Program of China (Grant No. 2021YFA1200202), the National Natural

Science Foundation of China (Grant No. 51931003) and the Hong Kong Research Grants Council (Grant No. GRF 11214121). The authors acknowledge the technical support from the Key Laboratory for Anisotropy and Texture of Materials of Ministry of Education, the State Key Laboratory of Rolling and Automation, Shi-changxu Innovation Center for Advanced Materials.

References

[1] X. Wu, Y. Zhu, Mater. Res. Lett. 5 (2017) 527–532.
[2] E. Ma, T. Zhu, Mater. Today 20 (2017) 323–331.
[3] X. Wu, M. Yang, F. Yuan, G. Wu, Y. Wei, X. Huang, Y. Zhu, Proc. Natl. Acad. Sci. U. S. A. 112 (2015) 14501–14505.
[4] Y. Yin, Q. Tan, Q. Sun, W. Ren, J. Zhang, S. Liu, Y. Liu, M. Bermingham, H. Chen, M.X. Zhang, J. Mater. Sci. Technol. 96 (2022) 113–125.
[5] Z. Li, X. Fang, Y. Wang, P. Jiang, J. Wang, C. Liu, X. Wu, Y. Zhu, C.C. Koch, Mater. Sci. Eng. A 777 (2020) 139074.
[6] X. Fang, G. He, X.M. Zheng, D. Kaoumi, Y. Li, Y. Zhu, Acta Mater. 186 (2020) 644–655.
[7] X. Bian, F. Yuan, Y. Zhu, X. Wu, Mater. Res. Lett. 5 (2017) 501–507.
[8] Y. Wang, C. Huang, M. Wang, Y. Li, Y. Zhu, Scr. Mater. 150 (2018) 22–25.
[9] J. Moering, X. Ma, J. Malkin, M. Yang, Y. Zhu, S. Mathaudhu, Scr. Mater. 122 (2016) 106–109.
[10] M.X. Yang, R.G. Li, P. Jiang, F.P. Yuan, Y.D. Wang, Y.T. Zhu, X.L. Wu, Mater. Res. Lett. 7 (2019) 433–438.
[11] F. Yuan, D. Yan, J. Sun, L. Zhou, Y. Zhu, X. Wu, Mater. Res. Lett. 7 (2018) 12–17.
[12] X. Wu, P. Jiang, L. Chen, J. Zhang, F. Yuan, Y. Zhu, Mater. Res. Lett. 2 (2014) 185–191.
[13] X. Ma, C. Huang, W. Xu, H. Zhou, X. Wu, Y. Zhu, Scr. Mater. 103 (2015) 57–60.
[14] J. Zhao, M. Zaiser, X. Lu, B. Zhang, C. Huang, G. Kang, X. Zhang, Int. J. Plast. 145 (2021) 103063.
[15] Y. Wang, M. Yang, X. Ma, M. Wang, K. Yin, A. Huang, C. Huang, Mater. Sci. Eng. A 727 (2018) 113–118.
[16] Y. Cao, Y. Wang, X. An, X. Liao, M. Kawasaki, S.P. Ringer, T.G. Langdon, Y. Zhu, Acta Mater. 63 (2014) 16–29.
[17] H. Ghassemi-Armaki, R. Maaß, S.P. Bhat, S. Sriram, J.R. Greer, K.S. Kumar, Acta Mater. 62 (2014) 197–211.
[18] D. Orlov, H. Fujiwara, K. Ameyama, Mater. Trans. 54 (2013) 1549–1553.
[19] C. Sawangrat, S. Kato, D. Orlov, K. Ameyama, J. Mater. Sci. 49 (2014) 6579–6585.
[20] S.K. Vajpai, M. Ota, Z. Zhang, K. Ameyama, Mater. Res. Lett. 4 (2016) 191–197.
[21] R. Zheng, G. Li, Z. Zhang, Y. Zhang, S. Yue, X. Chen, K. Ameyama, C. Ma, Mater. Res. Lett. 7 (2019) 217–224.
[22] Y. Zhu, K. Ameyama, P.M. Anderson, I.J. Beyerlein, H. Gao, H.S. Kim, E. Lavernia, S. Mathaudhu, H. Mughrabi, R.O. Ritchie, N. Tsuji, X. Zhang, X. Wu, Mater. Res. Lett. 9 (2020) 1–31.
[23] M. Kassner, P. Geantil, L.E. Levine, Int. J. Plast. 45 (2013) 44–60.
[24] C. Huang, Y. Wang, X. Ma, S. Yin, H.W. Höppel, M. Göken, X. Wu, H. Gao, Y. Zhu, Mater. Today 21 (2018) 713–719.
[25] Y. Wang, C. Huang, Y. Li, F. Guo, Q. He, M. Wang, X. Wu, R.O. Scattergood, Y. Zhu, Int. J. Plast. 124 (2020) 186–198.
[26] Y. Liu, Y. Cao, Q. Mao, H. Zhou, Y. Zhao, W. Jiang, Y. Liu, J.T. Wang, Z. You, Y. Zhu, Acta Mater. 189 (2020) 129–144.
[27] Y. Wang, C. Huang, Q. He, F. Guo, M. Wang, L. Song, Y. Zhu, Scr. Mater. 170 (2019) 76–80.
[28] X. Zhang, Y. Wang, N. Guo, Y. Wang, R. Li, C. Zhang, Y. Zhu, Eng. Fract. Mech. 237 (2020) 107244.
[29] M. Segolle, J. Santos, K.A. Kasvayee, A.E.W. Jarfors, J. Cast. Mater. Eng. 1 (2017) 33.
[30] J. Blaber, B. Adair, A. Antoniou, Exp. Mech. 55 (2015) 1105–1122.
[31] O. Muránsky, L. Balogh, M. Tran, C.J. Hamelin, J.S. Park, M.R. Daymond, Acta Mater. 175 (2019) 297–313.
[32] C. Zhu, T. Harrington, G.T. Gray, K.S. Vecchio, Acta Mater. 155 (2018) 104–116.
[33] T.J. Ruggles, D.T. Fullwood, J.W. Kysar, Int. J. Plast. 76 (2016) 231–243.
[34] B. Beausir, J.J. Fundenberger, ATEX - Software, Université de Lorraine - Metz, 2017 www.Atex-Software.Eu.
[35] J. Jiang, T.B. Britton, A.J. Wilkinson, Acta Mater. 61 (2013) 7227–7239.
[36] A.J. Wilkinson, D. Randman, Philos. Mag. 90 (2010) 1159–1177.
[37] X. Wu, P. Jiang, L. Chen, F. Yuan, Y.T. Zhu, Proc. Natl. Acad. Sci. U. S. A. 111 (2014) 7197–7201.
[38] X. Fang, Q. Xue, K. Yu, R. Li, D. Jiang, L. Ge, Y. Ren, C. Chen, X. Wu, Mater. Res. Lett. 8 (2020) 417–423.
[39] M. Yang, Y. Pan, F. Yuan, Y. Zhu, X. Wu, Mater. Res. Lett. 4 (2016) 145–151.
[40] D. Li, R.H. Wagoner, Acta Mater. 206 (2021) 116625.
[41] Y. Zhu, X. Wu, Prog. Mater. Sci. 131 (2023) 101019.
[42] M. Calcagnotto, D. Ponge, E. Demir, D. Raabe, Mater. Sci. Eng. A 527 (2010) 2738–2746.
[43] Y. Wang, C. Huang, Z. Li, X. Fang, M. Wang, Q. He, F. Guo, Y. Zhu, Extreme Mech. Lett. 37 (2020) 100686.
[44] M. Ardeljan, M. Knezevic, T. Nizolek, I.J. Beyerlein, N.A. Mara, T.M. Pollock, Int. J. Plast. 74 (2015) 35–57.
[45] M. Huang, C. Xu, G. Fan, E. Maawad, W. Gan, L. Geng, F. Lin, G. Tang, H. Wu, Y. Du, Acta Mater. 153 (2018) 235–249.